Thin Solid Films 622 (2017) 41–47

Contents lists available at ScienceDirect

Thin Solid Films

journal homepage: www.elsevier.com/locate/tsf

Tribocorrosion behaviors of CrN coating in 3.5 wt% NaCl solution

Qiang Chen [a], Yongzhi Cao [b,c], Zhiwen Xie [b,*], Tian Chen [d], Yuanyuan Wan [a], He Wang [b], Xu Gao [b], Yan Chen [b], Yanwen Zhou [b], Yuanyuan Guo [b]

[a] Southwest Technology and Engineering Research Institute, Chongqing 400039, China
[b] University of Science and Technology Liaoning, Anshan 114051, China
[c] Center for Precision Engineering, Harbin Institute of Technology, Harbin 150001, PR China
[d] Chongqing Institute of Green and Intelligent Technology, Chinese Academy of Sciences, Chongqing 400714, China

ARTICLE INFO

Article history:
Received 24 May 2016
Received in revised form 6 December 2016
Accepted 16 December 2016
Available online 18 December 2016

Keywords:
Stainless steel
CrN coating
Microstructure
Tribocorrosion
Plasma immersion ion implantation and deposition

ABSTRACT

Chromium nitride coatings are synthesized on the stainless steels by plasma immersion ion implantation and deposition. The microstructure and tribocorrosion behaviors of the as-deposited coatings are characterized by X-ray diffraction, X-ray photoelectron spectroscopy, scanning electron microscopy, transmission electron microscopy, reciprocating-sliding tribometer and electrochemical testing. The results show that the CrN coatings have a typical columnar growth structure consisting of face-centered cubic crystals. The CrN coatings greatly enhance the corrosion resistance and wear resistance of the stainless steel. However, frictional forces induce numerous micro-cracks which act as the diffusion channels for NaCl solution. Multi-scale Cl ion corrosion occurs simultaneously during the tribocorrosion and a force-corrosion synergy interaction induces the multi-degradation (e.g., intersecting cracks and layer delamination) of the CrN coating. The synergistic damage mechanisms of wear and corrosion are systematically discussed.

1. Introduction

Stainless steels are the most popular materials used in marine equipment (e.g., gears, shafts and propellers) because of their superior mechanical properties and excellent corrosion resistance [1–3]. However, the severe pitting corrosion and tribocorrosion damage of stainless steels greatly degrade their reliability and service life in marine environments [4–8]. It is necessary to fabricate a protective coating with excellent resistance against wear and corrosion.

The physical vapor deposited (PVD) nitrides and carbides have wide industrial applications as protective coatings in abrasive and corrosive environments because of their outstanding anti-wear and anti-corrosion properties [9–19]. For instance, the AISIH13 steels with a CrN coating presented an improved abrasive wear resistance in air atmosphere [10]. The CrN coatings greatly improved both erosion-corrosion performance in slurries [12] and the corrosion resistance of AISI304 steel in NaCl solution [13]. Moreover, TiCrN, TiB_xC_y/a-C, and CrCN coatings also exhibited qualities conducive to potential application in marine equipments because of their good corrosion resistance and wear resistance in seawater [14–18]. Tribocorrosion is the degradation of materials due to the simultaneous effects of mechanical wear and electrochemical corrosion in sliding contacts [20–24]. This synergistic effect is often more intense than wear and/or anodic dissolution alone [25]. Recently, Li [26] reported that a Ti–Si–N coating exhibited a higher wear rate in seawater than in air atmosphere. Wang [27] found that the wear loss of TiN and TiCN coatings in seawater was larger than that in air and distilled water. These results confirm that the wear-corrosion synergy interaction accelerates the failure of the PVD hard coatings. However, the synergistic damage mechanisms of wear and corrosion are still obscure. In this study, the tribocorrosion failure behaviors of hard CrN coatings in NaCl solution are investigated in detail. The effects of the wear-corrosion interaction on the tribological performances of the coatings are also discussed.

2. Materials and methods

CrN coatings were synthesized using a plasma immersion ion implantation and deposition facility [28–30]. AISI304 stainless steel was used for the substrate. All samples were mechanically polished by a diamond paste and ultrasonically washed with pure ethanol. Pure Cr metal was used as the target, with a working atmosphere of high-purity N_2. During the experiment, the vacuum chamber was evacuated to a base pressure of 0.005 Pa. Prior to the coating deposition, the polished samples were cleaned by Ar + sputtering at a bias voltage of 6 kV for 30 min to remove any residual pollutants, after which the CrN layer was deposited in a nitrogen atmosphere. The experimental parameters were displayed as follows: pressure, 0.3 Pa; bias voltage, 20 kV; frequency, 75 Hz; bias voltage duration, 60 μs; and deposition time, 3 h.

* Corresponding author at: No. 185, Qianshan Midroad, Hi-Tech Zone, Anshan, Liaoning, China.
E-mail address: xzwustl@126.com (Z. Xie).

http://dx.doi.org/10.1016/j.tsf.2016.12.023
0040-6090/

The phase composition of the coatings was examined by X-ray diffraction (XRD, X'pert Powder, PANalytical, Holland) using a Cu-Kα radiation source. The diffraction angle measurement ranged from 20 to 90° at a scanning rate of 0.1°/s. The test was conducted at an incidence angle of 0.8°, a voltage of 40 kV, and a current of 40 mA, using a step size of 0.05° and an integration time of 0.5 s/step. The chemical bonding states of the coating were detected by X-ray photoelectron spectroscopy (XPS, K-Alpha, Thermo Fisher Scientific, Inc., USA) using Al-Kα radiation as the excitation source. Argon ion etching was performed to remove contaminants at an accelerating voltage of 1000 eV. Field-emission scanning electron microscopy (FESEM, JSM-6701F, JEOL, Japan) was employed to observe the cross-sectional morphologies of the coating. The cross-section microstructure of the coating was observed by transmission electron microscopy (TEM, FEI-Tecnai-30, USA) with an acceleration voltage of 300 kV. The mechanical properties of the coating and substrate were evaluated by using a nano-indentation system (Nano Indenter G200, Keysight, USA). The indentation test was carried out in the continuous loading mode. The maximum displacement depth was 2000 nm and twenty indentations were conducted in each sample. To minimize the negative effect of a surface modification layer originating from mechanical polishing, the actual mechanical property of the substrate was also evaluated by using Brinell testing (HB-3000, Laizhou Laihua Testing Instrument Factory, China). The indenter was a quenched steel ball ($\Phi = 10$ mm), with a load and holding time of 3000 kg and 30 s, respectively. The corrosion behaviors of the coating were investigated by electrochemical testing (PGSTAT302N, Switzerland). High-purity platinum was used for the counter electrode, while the sample was the working electrode (1 cm^2 exposed area) with a saturated calomel electrode (SCE) as the reference electrode. The test was carried out in a 3.5-wt% NaCl solution. The electrochemical tests were conducted under the potentiostatic mode. The potential range and scanning rate were ±250 mV and 1 mV/s, respectively. The tests were performed three times to ascertain reproducibility. A reciprocating-sliding tribometer and a three electrode cell configuration (MFT-R4000, Lanzhou Institute of Chemical Physics, Chinese Academy of Sciences, China) were employed to evaluate the tribocorrosion behaviors of the coating in a 3.5-wt% NaCl solution. As shown in Fig. 1, high-purity graphite was used as the counter electrode, with the sample and a SCE used as the working and reference electrodes, respectively. For tribocorrosion under open-circuit potential (OCP) conditions, the OCP was recorded for 5 min before a 15-min sliding test was performed. A 5 N load was applied on the sample through an Al_2O_3 ball ($\Phi =$ 6 mm). The amplitude and frequency were 5 mm and 0.1 Hz, respectively. The OCP recording continued for 5 min until the sliding was ended. Each test was repeated three times under the same conditions in order to check the reproducibility. The corrosion and wear track morphologies with corresponding compositional analyses were examined by SEM.

3. Results and discussion

Fig. 2 shows the XRD pattern of the substrate and CrN coating. According to the Joint Committee on Powder Diffraction Standards (JCPDS)-330397, the reflection angles of the substrate centered at 43.65°, 50.76°, and 74.58° are associated with the (111), (200), and (220) planes of γ-Fe in the austenitic phase. The Bragg refection angles of the CrN coating located at 37.61°, 43.69°, 63.51°, and 76.22°, referring to the JCPDS-762494, are assigned to face-centered cubic CrN (111), (200), (220), and (311) planes, respectively.

Fig. 3 presents the chemical binding states of Cr and N in the CrN coating. As shown in Fig. 3a, the Cr $2p_{3/2}$ peak centered at the binding energy of 575.2 eV can be attributed to the presence of CrN [31–33]. The binding energy of the N1 s peak located at 396.9 eV (see Fig. 3b), which can also be associated with CrN [31–33].

Fig. 4a shows the cross-sectional SEM image of the CrN coating. This coating exhibits a typical columnar growth structure (marked by arrows), without cracks or coating delamination, indicating good coating quality and high adhesion strength. The thickness of the coating was ~1.39 μm. The atomic force microscopy (AFM) surface image shown in Fig. 4b reveals that the CrN coating exhibited a smooth and uniform morphology with a roughness (Ra) of 5.3 nm. Visible grain boundaries were observed in the AFM image, which agrees well with the columnar growth of this coating (Fig. 4a).

Fig. 5 shows the cross-sectional TEM images of the CrN coating. Arrows indicate the direction of the coating growth. As seen in Fig. 5a, the bright-field image of the CrN coating shows typical columnar crystallites perpendicular to the substrate surface. A high-resolution TEM (HRTEM) lattice image shown in Fig. 5b reveals that the nanoscale crystal grains can be seen and the (200) plane of cubic CrN can be identified in the coating. According to the XRD, XPS, SEM and TEM results, it can be concluded that the CrN coatings were successfully fabricated on the stainless steel.

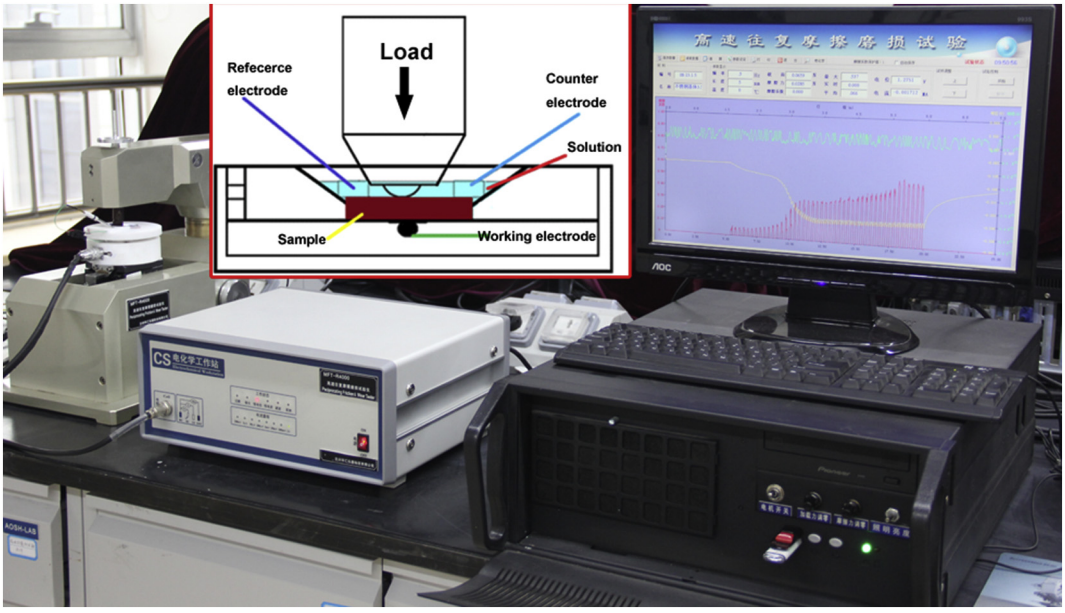

Fig. 1. The scheme of the tribocorrosion apparatus.

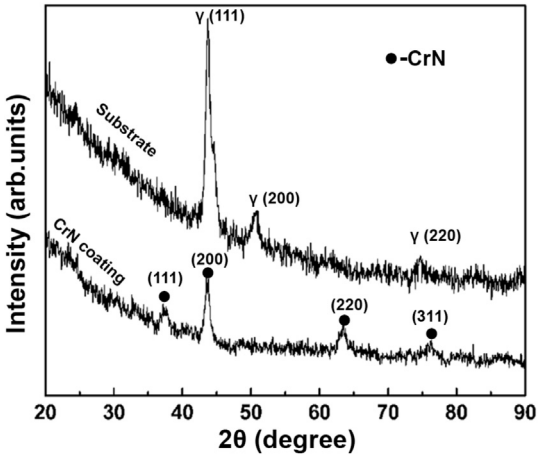

Fig. 2. XRD pattern of the substrate and CrN coating.

Fig. 6 shows the anode polarization curves of the substrate and CrN coating. As shown in Fig. 6a, the substrate had a corrosion potential of -317 ± 43 mV and a corrosion current density of $1.64 \pm 0.31 \times 10^{-7}$ A/cm^2. In comparison, the CrN coating exhibited a better corrosion resistance with a higher corrosion potential of -168 ± 32 mV and a lower corrosion current density of $3.21 \pm 0.23 \times 10^{-8}$ A/cm^2 (Fig. 6b). The corrosion morphologies of all samples are shown in Fig. 7. Numerous pitting corrosion pores can be observed on the substrate's surface (Fig. 7a). However, the CrN coating exhibited excellent corrosion resistance with a smooth morphology (Fig. 7b).

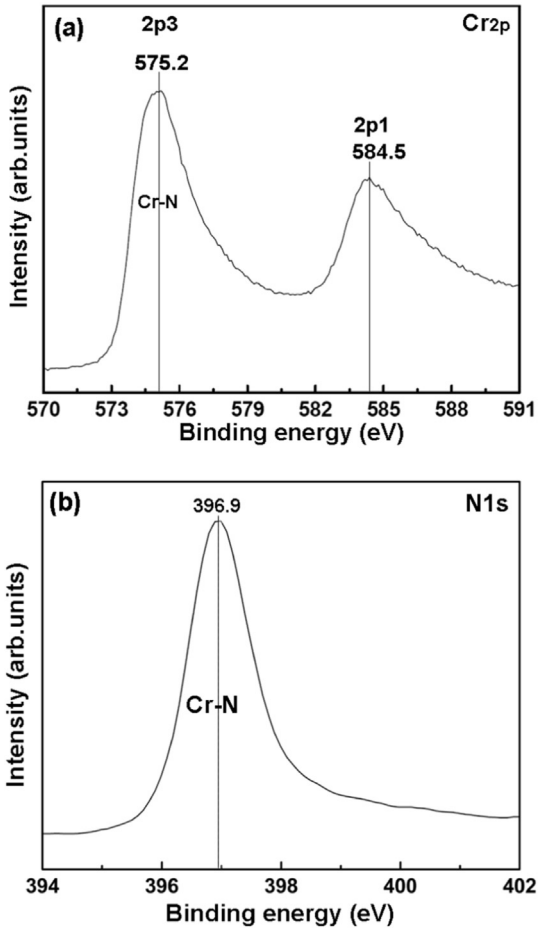

Fig. 3. XPS spectrum of the CrN coating: (a) Cr 2p, (b) N 1 s.

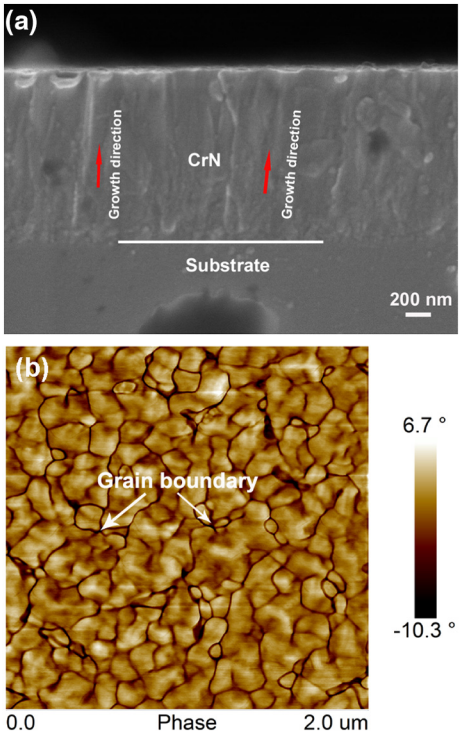

Fig. 4. Cross-sectional SEM image (a) and surface AFM morphology (b) of the CrN coating.

Electrochemical testing confirms that the CrN coating provided excellent corrosion protection for the stainless steel substrate.

Fig. 8a shows the typical hardness–displacement curves of the substrate and CrN coating. The untreated substrate exhibited a hardness of 2.58 ± 0.12 GPa at a displacement depth of 2000 nm. In comparison, the CrN coating demonstrated a higher hardness of 35.43 ± 5.74 GPa.

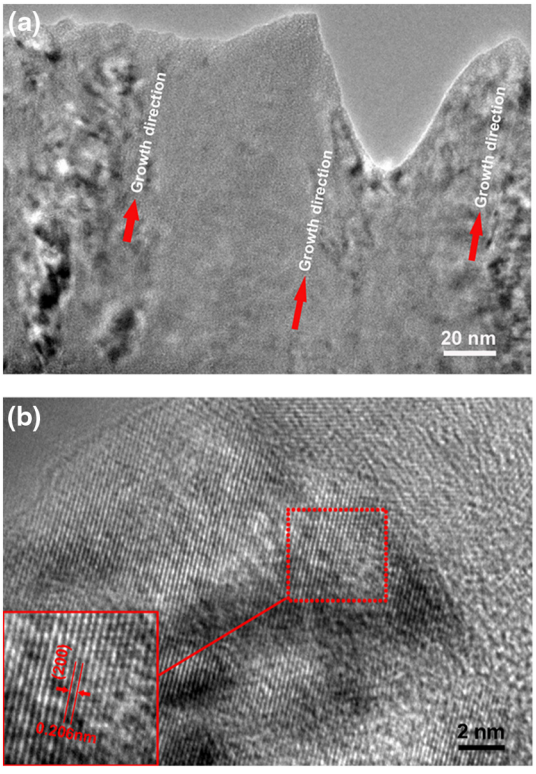

Fig. 5. Cross-sectional TEM images of the CrN coating: (a) Bright field, (b) HRTEM lattice image.

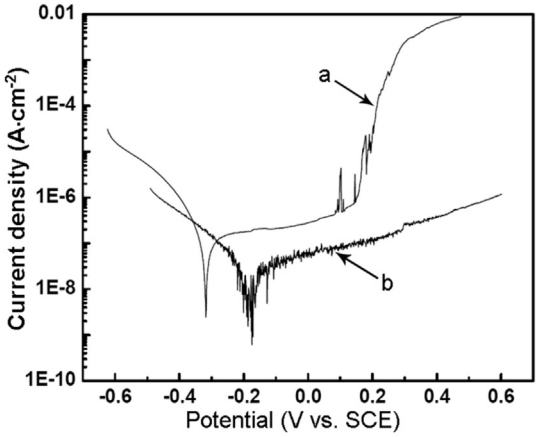

Fig. 6. Polarization curves of all samples: (a) substrate, (b) CrN coating.

The Brinell testing revealed that the actual hardness of the substrate was 161 ± 8 HBS (Fig. 8b). These hardness characterizations confirm that the fabrication of the CrN coating on stainless steel greatly improved its surface mechanical properties.

Fig. 9a presents the friction curve of the CrN coating in air atmosphere. It can be seen that the friction coefficient increased gradually at the initial stage and approached a stable value of 0.53 as the sliding time exceeded 9 min. In comparison, the CrN coating exhibited an unstable friction coefficient during the entire tribocorrosion, as shown in Fig. 9b, with the friction coefficient increasing rapidly from 0.05 to 0.45 as the sliding time continued for 3 min, reaching its highest value of 0.61 when the sliding time reached 12 min. The corresponding OCP curve in Fig. 9b shows that the CrN coating exhibited a relatively stable OCP value during soaking, but the OCP value decreased markedly during tribocorrosion and increased gradually during passivation. The evolution of the OCP value confirms that the force-corrosion synergy interaction occurred during the tribocorrosion test.

Fig. 10 shows the plan-view SEM images with the cross-sectional profiles of the wear track after the sliding test. As shown in Fig. 10a, the CrN coating exhibited a very smooth wear track in air atmosphere with a width of 187 μm and a depth of 521 nm. In comparison, the CrN coating suffered from severe tribocorrosion damage in NaCl solution with a wider and deeper wear track profile (249 μm and 978 nm, respectively); a large amount of coating facture and delamination were observed on the wear track surface (Fig. 10b).

Fig. 11 shows the plan-view SEM image with energy dispersive spectroscopy (EDS) analysis of the wear track after the sliding test in air atmosphere. It can be seen that numerous parallel cracks were observed on the wear track surface. The corresponding EDS analysis reveals that

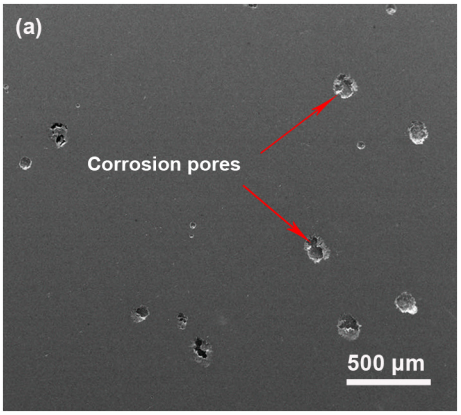

Fig. 7. Corrosion morphologies of all samples: (a) substrate, (b) CrN coating.

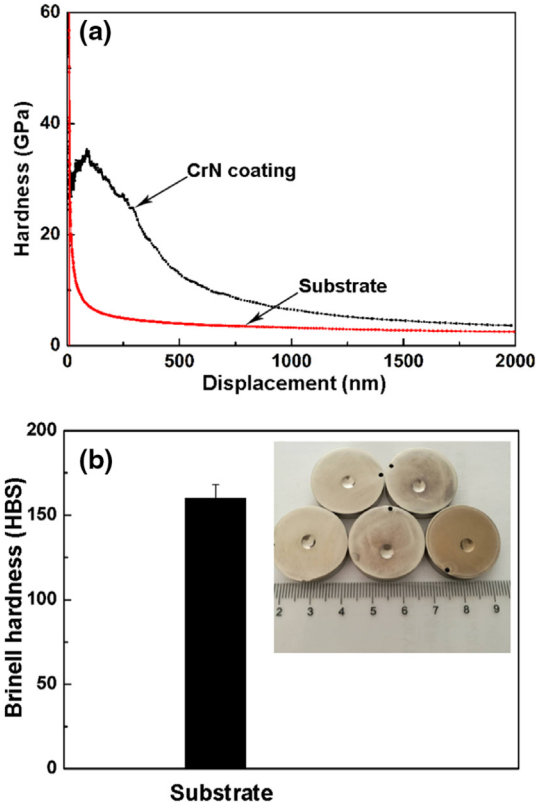

Fig. 8. (a) Hardness–displacement curve of the substrate and CrN coating; (b) Brinell hardness of the substrate.

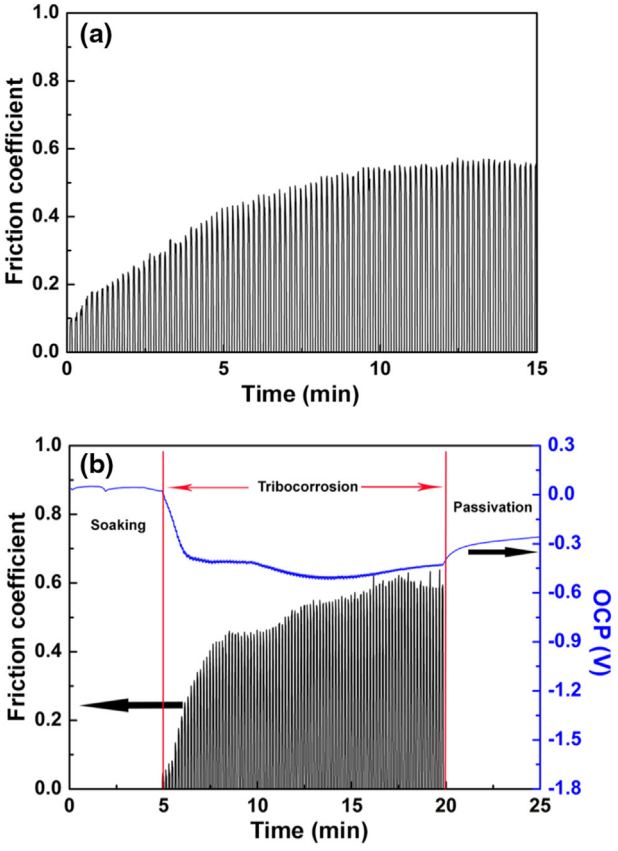

Fig. 9. (a) Friction curve of the CrN coating in air atmosphere; (b) Tribocorrosion curve with the corresponding OCP of the CrN coating in NaCl solution.

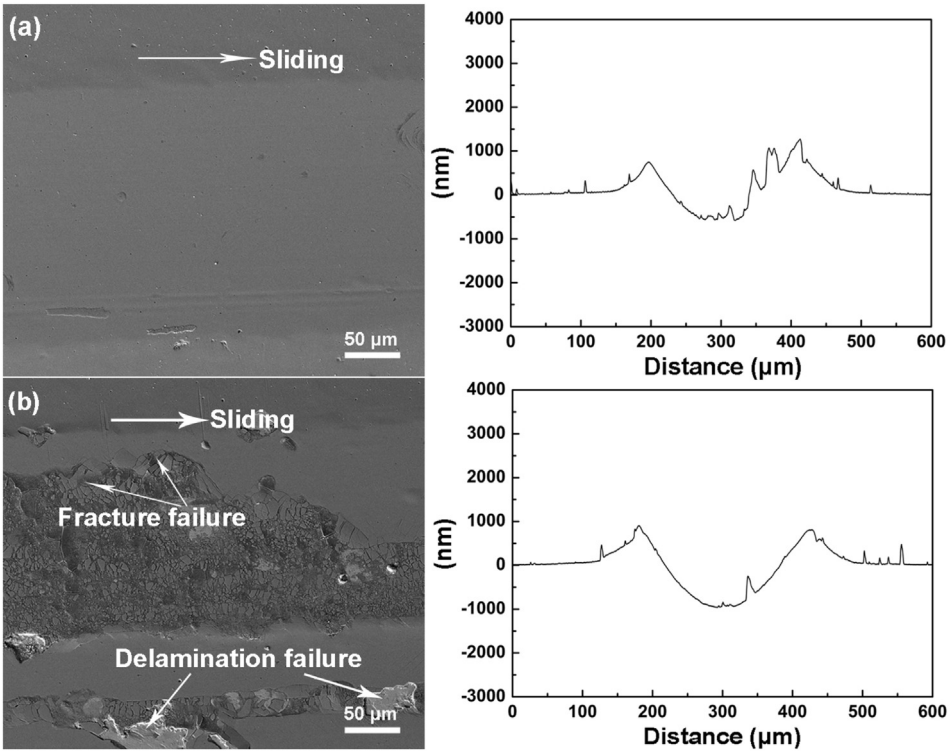

Fig. 10. Plan-view SEM images with the cross-sectional profiles of the wear track after the sliding test: (a) in air atmosphere, (b) in NaCl solution.

strong Cr element peaks were identified, indicating that this coating was not worn to failure.

Fig. 12 presents the plan-view SEM image with the EDS analysis of the wear track after the tribocorrosion test. As shown in Fig. 12a, visible layered delamination appears on the wear track. A number of intersecting cracks are distributed at the edges of the failure zone. The EDS analysis reveals that strong Cr elements were detected in zone A (Fig. 12b), which is consistent with the results seen in Fig. 11. The EDS analysis also proves that Fe, Cr, Ni, Si, and Cl elements were detected in zone B (Fig. 12c), implying that the delamination failure occurred at the coating/substrate interface. The high-resolution SEM image (the inset in Fig. 12c) reveals that a visible micropore appeared in the failure zone, indicating serious pitting corrosion. In addition, the EDS spectrum shows that Cr and Cl elements were identified in zone C (Fig. 12d). The high-resolution SEM image in Fig. 11d shows the presence of serious coating fractures on the wear track. These failure characteristics are obviously different from the wear track morphology seen in Fig. 11.

Apparently, the as-deposited CrN coating exhibited a better wear performance in the air atmosphere than in the NaCl solution. This tribological property evolution can be attributed to the force-corrosion synergy interaction. As shown in Fig. 4, the columnar growth of the CrN coating benefited the microcrack initiation and propagation along the columnar boundaries. The frictional force induced many microcracks during the sliding test (Fig. 11). These cracks acted as a diffusion channel and accelerated the diffusion of the NaCl solution in the coating. Many researchers have reported that Cl ions are the key factor to induce pitting corrosion failure in these materials [4–5]. In this study, visible pitting corrosion pores and Cl elements were identified in the failure zone of the wear track (see Fig. 12), indicating that Cl ion corrosion occurred simultaneously during the tribocorrosion. Most importantly, this multiscale Cl ion corrosion greatly deteriorated the interfacial bonding strength between the adjacent columnar crystals. Force-corrosion synergy damage induced the multi-degradation failure of the CrN coating due to the weakening interfacial strength. As a result, layer

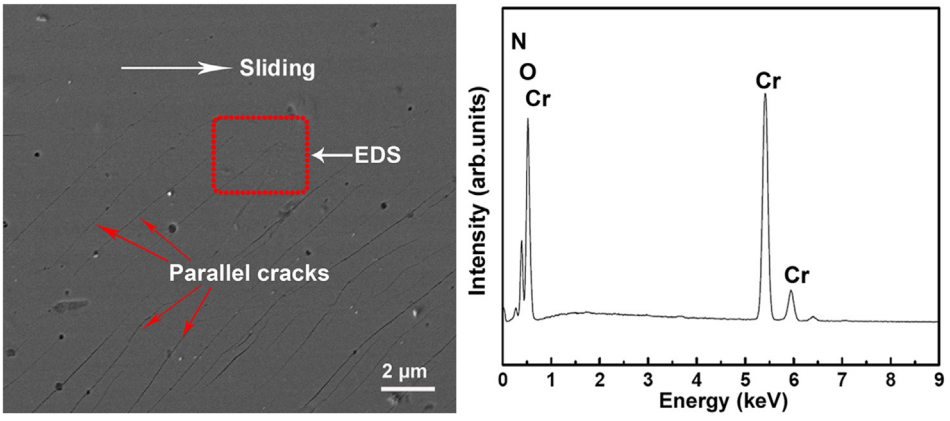

Fig. 11. Plan-view SEM images with the EDS analysis of the wear track after the sliding test in air atmosphere.

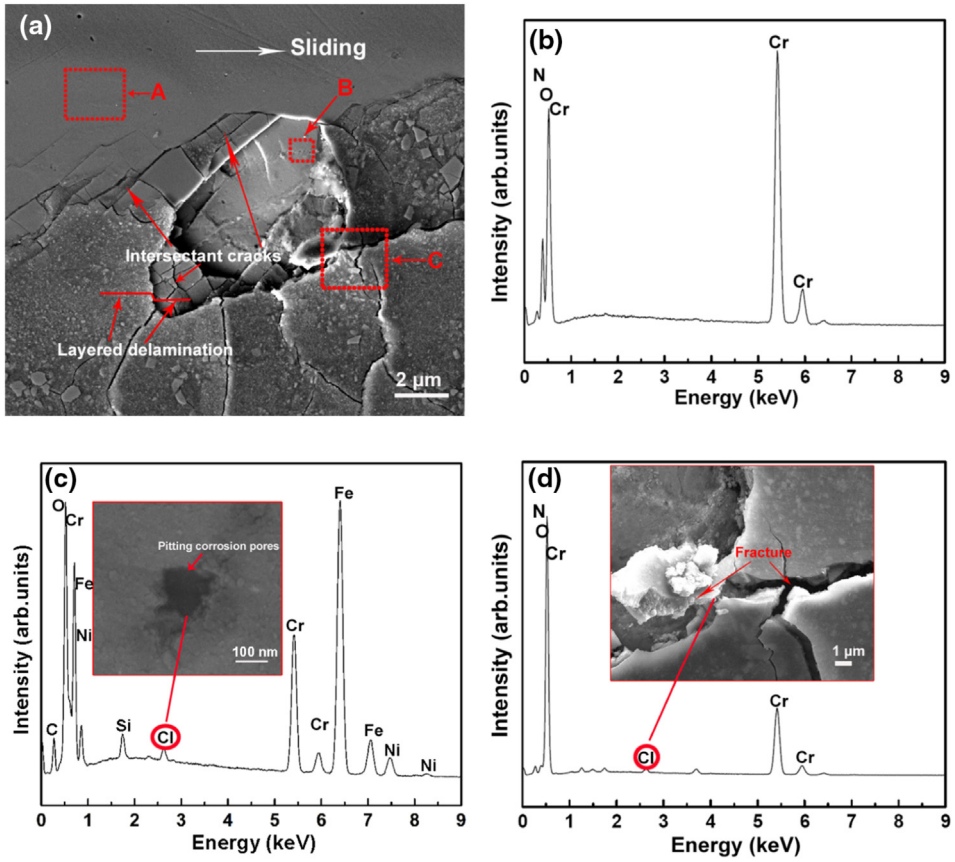

Fig. 12. (a) Plan-view SEM images of the wear track after the tribocorrosion test, (b) EDS analysis in zone A, (c) EDS analysis in zone B, (d) EDS analysis in zone C.

delamination and a large number of intersecting cracks were observed on the wear track surface (Fig. 12a).

4. Conclusions

This study investigated the tribocorrosion failure behaviors of the CrN coating synthesized by plasma immersion ion implantation and deposition. The main conclusions are listed as follows:

(1) The as-deposited CrN coating showed a typical columnar growth structure and crystallized in the face-centered cubic structure.
(2) The as-deposited CrN coating showed superior corrosion resistance in NaCl solution and excellent wear resistance in air atmosphere, but exhibited poor tribocorrosion resistance in NaCl solution.
(3) The frictional force induced many microcracks in the CrN coating. These microcracks acted as the diffusion channels for the NaCl solution and lead to multiscale Cl ion corrosion.
(4) The force-corrosion synergy interaction induced a multi-degradation failure of the CrN coating during tribocorrosion because the multiscale Cl ion corrosion weakened the interfacial bonding strength between the adjacent columnar crystals.

Acknowledgement

This work is supported by National Natural Science Foundation of China (No. 51401201, 51502126 and 21573054), Natural Science Foundation of Liaoning Province (201602392), Liaoning BaiQianWan Talents Program (201571), Program for Liaoning Excellent Talents in University (LJQ2015052), Excellent Talents Program of University of Science and Technology Liaoning (2014RC04) and Chongqing Research of Application Foundation and Advanced Technology (cstc2014jcyjA50009). We gratefully acknowledge Prof. L. P. Wang, Harbin Institute of Technology, for helpful discussion and contribution on coating deposition.

References

[1] Z.H. Jin, H.H. Ge, W.W. Lin, Y.W. Zong, S.J. Liu, J.M. Shi, Corrosion behaviour of 316L stainless steel and anti-corrosion materials in a high acidified chloride solution, Appl. Surf. Sci. 322 (2014) 47–56.
[2] M. Naghizadeh, D. Nakhaie, M. Zakeri, M.H. Moayed, The effect of dichromate ion on the pitting corrosion of AISI 316 stainless steel part II: Pit initiation and transition to stability, Corros. Sci. 94 (2015) 420–427.
[3] W. Pacquentin, N. Carona, R. Oltra, Effect of microstructure and chemical composition on localized corrosion resistance of a AISI 304L stainless steel after nanopulsed-laser surface melting, Appl. Surf. Sci. 356 (2015) 561–573.
[4] Y. Wang, G. Cheng, W. Wu, Q. Qiao, Y. Li, X. Li, Effect of pH and chloride on the micro-mechanism of pitting corrosion for high strength pipeline steel in aerated NaCl solutions, Appl. Surf. Sci. 349 (2015) 746–756.
[5] J. Bhandari, F. Khan, R. Abbassi, V. Garaniy, R. Ojeda, Modelling of pitting corrosion in marine and off shore steel structures-A technical review, J. Loss Prev. Process Ind. 37 (2015) 39–62.
[6] C.B. von der Ohe, R. Johnsen, N. Espallargas, Multi-degradation behavior of austenitic and super duplex stainless steel - the effect of 4-point static and cyclic bending applied to a simulated seawater tribocorrosion system, Wear 288 (2012) 39–53.
[7] R.C.C. Silva, R.P. Nogueira, I.N. Bastos, Tribocorrosion of UNS S32750 in chloride medium: effect of the load level, Electrochim. Acta 56 (2011) 8839–8845.
[8] A. López, R. Bayón, F. Pagano, A. Igartua, A. Arredondo, J.L. Arana, J.J. González, Tribocorrosion behaviour of mooring high strength low alloy steels in synthetic seawater, Wear 338–339 (2015) 1–10.
[9] R. Niu, J. Li, Y. Wang, J. Chen, Q. Xue, Structure and tribological behavior of GLCH/nitride coupled coatings on Ti6Al4V by nitriding and magnetron sputtering, Diam. Relat. Mater. 64 (2016) 70–79.
[10] M. Vite, M. Moreno-Ríos, E.A. Gallardo Hernández, J.R. Laguna-Camacho, A study of the abrasive resistance of sputtered CrN coatings deposited on AISI316 and AISI H13 steel substrates using steel particles, Wear 271 (2011) 1273–1279.
[11] L. Shan, Y. Wang, J. Li, X. Jiang, J. Chen, Improving tribological performance of CrN coatings in seawater by structure design, Tribol. Int. 82 (2015) 78–88.
[12] J.A. Alegría-Ortega, L.M. Ocampo-Carmona, F.A. Suárez-Bustamante, J.J. Olaya-Flórez, Erosion–corrosion wear of Cr/CrN multi-layer coating deposited on AISI-304 stainless steel using the unbalanced magnetron (UBM) sputtering system, Wear 290–291 (2012) 149–153.

[13] A. Ruden, E. Restrepo-Parra, A.U. Paladines, F. Sequeda, Corrosion resistance of CrN thin films produced by dc magnetron sputtering, Appl. Surf. Sci. 270 (2013) 150–156.
[14] S. Rossi, L. Fedrizzi, M. Leoni, P. Scardi, Y. Massiani, (Ti, Cr)N and Ti/TiN PVD coatings on 304 stainless steel substrates: wear-corrosion behaviour, Thin Solid Films 350 (1999) 161–167.
[15] S.A. Naghibi, K. Raeissi, M.H. Fathi, Corrosion and tribocorrosion behavior of Ti/TiN PVD coating on 316L stainless steel substrate in Ringer's solution, Mater. Chem. Phys. 148 (2014) 614–623.
[16] Y. Ye, Y. Wang, H. Chen, J. Li, Y. Yao, C. Wang, Doping carbon to improve the tribological performance of CrN coatings in seawater, Tribol. Int. 90 (2015) 362–371.
[17] E. Gracia-Escosa, I. García, J.C. Sánchez-López, M.D. Abad, A. Mariscal, M.A. Arenas, J. de Damborenea, A. Conde, Tribocorrosion behavior of TiBxCy/a-C nanocomposite coating in strong oxidant disinfectant solutions, Surf. Coat. Technol. 263 (2015) 78–85.
[18] Y. Ye, Y. Wang, C. Wang, J. Li, Y. Yao, An analysis on tribological performance of CrCN coatings with different carbon contents in seawater, Tribol. Int. 91 (2015) 131–139.
[19] T. Suna, N. Xue, C. Liu, C. Wang, J. He, Bioactive (Si, O, N)/(Ti, O, N)/Ti composite coating on NiTi shapememory alloy for enhanced wear and corrosion performance, Appl. Surf. Sci. 356 (2015) 599–609.
[20] Y. Sun, V. Ran, Tribocorrosion behaviour of AISI 304 stainless steel in 0.5 M NaCl solution, Mater. Chem. Phys. 129 (2011) 138–147.
[21] E. Lemaire, M. Le Calvar, Evidence of tribocorrosion wear in pressurized water reactors, Wear 249 (2001) 338–344.
[22] S. Mischler, Triboelectrochemical techniques and interpretation methods in tribocorrosion: a comparative evaluation, Tribol. Int. 41 (2008) 573–583.
[23] Y. Sun, R. Bailey, Improvement in tribocorrosion behavior of 304 stainless steel by surface mechanical attrition treatment, Surf. Coat. Technol. 253 (2014) 284–291.
[24] Y.N. Kok, R. Akid, P.E. Hovsepian, Tribocorrosion testing of stainless steel (SS) and PVD coated SS using a modified scanning reference electrode technique, Wear 259 (2005) 1472–1481.
[25] D. Landolt, S. Mischler, M. Stemp, Electrochemical methods in tribocorrosion: a critical appraisal, Electrochim. Acta 46 (2001) 3913–3929.
[26] Y. Yao, J. Li, Y. Wang, Y. Ye, L. Zhu, Influence of the negative bias in ion plating on the microstructural and tribological performances of Ti–Si–N coatings in seawater, Surf. Coat. Technol. 280 (2015) 154–162.
[27] L. Shan, Y. Wang, J. Li, L. He, X. Wu, J. Chen, Tribological behaviours of PVD TiN and TiCN coatings in artificial seawater, Surf. Coat. Technol. 226 (2013) 40–50.
[28] G. Wang, Z. Xie, T. Chen, Z. Chen, X. Song, G. Xu, X. Yu, H. Song, Electrochemical behavior of TiAlSiN hard coatings synthesized by a multi-plasma immersion ion implantation and deposition technique, Thin Solid Films 584 (2015) 222–227.
[29] L.P. Wang, L. Huang, Z.W. Xie, X.F. Wang, B.Y. Tang, Fourth-generation plasma immersion ion implantation and deposition facility for hybrid surface modification l Ayer fabrication, Rev. Sci. Instrum. 79 (2008) 023306.
[30] T. Chen, Z. Xie, F. Gongb, Z. Luo, Z. Yang, Correlation between microstructure evolution and high temperature properties of TiAlSiN hard coatings with different Si and Al content, Appl. Surf. Sci. 314 (2014) 735–745.
[31] W. Zhongzhen, X. Tian, C. Gong, S. Yang, P.K. Chu, Micrograph and structure of CrN films prepared by plasma immersion ion implantation and deposition using HPPMS plasma source, Surf. Coat. Technol. 229 (2013) 210–216.
[32] A. Lippitz, T. Hübert, XPS investigations of chromium nitride thin films, Surf. Coat. Technol. 200 (2005) 250–253.
[33] P.L. Tam, Z.F. Zhou, P.W. Shum, K.Y. Li, Structural, mechanical, and tribological studies of Cr–Ti–Al–N coating with different chemical compositions, Thin Solid Films 516 (2008) 5725–5731.